single wavelength and linear polarization have been successfully achieved. In the case of the other lasers (VCSEL or CGSEL), when the area of the laser cavity becomes very large, the lateral mode becomes multimode because no mechanism for lateral mode control is present, leading to multimodal lasing in terms of wavelength and polarization. Also, the near-field pattern extends to the long-axis direction of individual elliptical unit cells. The lasing is considered to occur at either band edge II′ or III′ (Fig. 3) when we compare the obtained near-field pattern and the polarization with the results shown in Fig. 3, B through E. As the Poynting vector is directed toward the long axis of elliptical unit cells in band edge II′ or III′, the near-field pattern spread in only one direction. All the measured elliptical devices lased in the same manner. In separately fabricated 2D PCs with circular unit cells, the observed near-field patterns extended in two perpendicular directions, rendering control of the polarization mode very difficult. On the basis of these results, the deformation of the unit cell structure in 2D PC lattice constitutes an effective means of controlling the polarization mode of PC surface emission.

References and Notes

1. E. Yablonovitch, *J. Opt. Soc. Am. B* **10**, 283 (1993).
2. S. John, *Phys. Today* **44**, 32 (1991).
3. N. Vats, S. John, *Phys. Rev. A* **58**, 4168 (1998).
4. J. D. Joannopoulos, P. R. Villeneuve, S. Fan, *Nature* **386**, 143 (1997).
5. S. Noda, K. Tomoda, N. Yamamoto, A. Chutinan, *Science* **289**, 604 (2000).
6. S. Noda, M. Imada, A. Chutinan, *Nature* **407**, 608 (2000).
7. O. Painter *et al.*, *Science* **284**, 1819 (1999).
8. M. Imada *et al.*, *Appl. Phys. Lett.* **75**, 316 (1999).
9. M. Meyer *et al.*, *Appl. Phys. Lett.* **74**, 7 (1999).
10. For example, S. Uchiyama, K. Iga, *IEEE J. Quantum Electron.* **QE-22**, 301 (1986).
11. For example, C. M. Wu *et al.*, *IEEE Photon. Tech. Lett.* **4**, 960 (1992).
12. M. Imada, A. Chutinan, S. Noda, M. Mochizuki, *Phys. Rev. B*, in preparation.
13. M. Yokoyama, S. Noda, unpublished data.
14. Web figure 1 is available at *Science* Online at www.sciencemag.org/cgi/content/full/293/5532/1123/DC1.

15. Supported in part by a grant-in-aid for scientific research of priority areas from the Ministry of Education, Culture, Sports, Science, and Technology of Japan; Kyoto University VBL; and ICF Foundation.

19 April 2001; accepted 5 July 2001

High-Temperature Ferromagnetism in CaB_2C_2

J. Akimitsu,[1,2]* K. Takenawa,[1] K. Suzuki,[3] H. Harima,[4] Y. Kuramoto[5]

We report a high Curie–temperature ferromagnet, CaB_2C_2. Although the compound has neither transition metal nor rare earth ions, the ferromagnetic transition temperature T_c is about 770 Kelvin. Despite this high T_c, the magnitude of the ordered moment at room temperatures is on the order of 10^{-4} Bohr magneton per formula unit. These properties are rather similar to those of doped divalent hexaborides, such as $Ca_{1-x}La_xB_6$. The calculated electronic states also show similarity near the Fermi level between CaB_2C_2 and divalent hexaborides. However, there is an important difference: CaB_2C_2 crystallizes in a tetragonal structure, and there are no equivalent pockets in the energy bands for electrons and holes—in contrast with CaB_6. Thus, the disputed threefold degeneracy, specific to the cubic structure, in the energy bands of divalent hexaborides turns out not to be essential for high-temperature ferromagnetism. It is the peculiar molecular orbitals near the Fermi level that appear to be crucial to the high-T_c ferromagnetism.

The search for magnets with high ferromagnetic transition temperatures (T_c's) is not only of practical interest but is also of basic scientific interest, in identifying the mechanism. The origin of the high-T_c ferromagnetism observed in doped hexaborides was initially attributed to electron correlations in the low-density electron gas (*1*), and much attention has been paid to the band structure of the divalent hexaborides (*2*, *3*). It has been postulated that the presence of three equivalent valleys in the energy bands plays an important role in the formation of excitonic ferromagnetism (*4*–*6*). However, the fact that this has been observed only in this particular class of compounds has caused difficulty in identifying the mechanism of this phenomenon. This study reveals that the high-T_c ferromagnetism is not a singular phenomenon but that a similar ferromagnetism appears in a tetragonal compound, CaB_2C_2, without the band degeneracy. Our observation may provide a route for preparation of new high-T_c ferromagnets.

Powder samples of CaB_2C_2 were prepared from Ca shot (99%), amorphous powder boron (99%), and powder carbons (99%). The starting materials were mixed at the stoichiometric ratio Ca:B:C = 1: 2:2 in an argon glovebox, pressed into pellets, and placed in a wrapped tantalum tube. The pellets were then heated in two ways: (i) at 1050°C for 20 hours in 2000 atm of an argon atmosphere in a hot isostatic-pressing furnace, and (ii) at 1050°C for 30 hours in a vacuum quartz tube. In both cases, reddish-brown powders of CaB_2C_2 were obtained. Because the samples are sensitive to moisture, they were handled under an argon atmosphere.

In the x-ray diffraction patterns obtained (Fig. 1), most of the diffraction peaks can be indexed to the tetragonal structure, consistent with an earlier structural study (*7*) of CaB_2C_2. There are slight amounts of impurity phases of CaO and CaB_6 in the sample, as seen in the corresponding weak intensity. The inset of Fig. 1 shows the two-dimensional network formed by boron (B) and carbon (C) atoms in CaB_2C_2. The Ca ions sit on each vertex and center of the square and sandwich each B-C layer. Depending on the stacking of B-C layers along the *c* axis, the crystal symmetry becomes either simple tetragonal (*P*4/*mbm*) lattices or body-centered tetragonal (*I*4/*mcm*) lattices. The latter has the sequence B-C-B-C- . . . along the *c* axis, whereas the former has B-B- . . . (and C-C- . . .) stacking. Experimentally, these two different structures can be distinguished only by observing a signal corresponding to the B-C superstructure along the *c* axis. Unfortunately, the x-ray scattering intensity is too weak to identify or disprove such a signal. Hence, the crystal structure of CaB_2C_2 has not yet been experimentally fixed. On the other hand, it has been established that related compounds RB_2C_2 with trivalent rare earth ion R have *P*4/*mbm* (*8*, *9*).

Magnetization measurements with a SQUID magnetometer (Fig. 2, inset) show the magnetization versus applied magnetic fields at $T = 5$ K. The diamagnetic contribution of the sample holder was independently measured by removing the sample, and this background has been subtracted. The magnetization shows a characteristic feature of ferromagnetism, with the saturation moment of 3.8×10^{-4} Bohr magneton (μ_B) per formula unit [or 2.1 electromagnetic units (emu) per mole of formula] at 1 T, which is comparable

[1]Department of Physics, Aoyama-Gakuin University, Tokyo 157–8572, Japan. [2]Core Research for Evolutional Science and Technology (CREST) of the Japan Science and Technology Corporation, Japan. [3]Faculty of Environmental and Information Sciences, Yokohama National University, Yokohama 240–8501, Japan. [4]Institute of Scientific and Industrial Research, Osaka University, Osaka 567-0047, Japan. [5]Department of Physics, Tohoku University, Sendai 980-8578, Japan.

*To whom correspondence should be addressed. E-mail: jun@phys.aoyama.ac.jp

to that in divalent hexaborides (*1*). The observed hysteresis is consistent with ferromagnetism. The magnetization at room temperature is almost the same as that at $T = 5$ K. The magnetization as a function of temperature (Fig. 2) reveals that the Curie temperature T_c is high and is estimated to be 770 K. The observed magnitude of the ferromagnetic moment is of the same order as that in CaB_6, and the Curie temperature is different from the transition temperature reported for the doped CaB_6 (*1*). These facts exclude the possibility that the observed ferromagnetism is due to the slight amount of CaB_6 present as an impurity phase. Therefore, the observed ferromagnetism is intrinsic in the sample of CaB_2C_2.

The ferromagnetism observed here in CaB_2C_2 is very similar to that found in doped hexaborides. The unique band structures in the host divalent hexaborides seem to be important for the weak ferromagnetism (*2*–*6*). The conventional local density approximation (LDA) calculations predict that the host material CaB_6 is a poor conductor that has a small overlap or a small gap between valence and conduction bands at the three X points in the Brillouin zone (*2*, *3*). Recently, partial inclusion of a correlation effect in the Green's function description, known as the GW approximation, has pointed to a semiconducting band structure with a band gap of 0.8 eV in CaB_6 (*10*). It is natural to inquire into the band structure of CaB_2C_2. The resistivity reported in (*7*) shows a semiconducting behavior with an energy gap of 0.2 eV. In deducing the intrinsic energy band structure from experiment, one should take notice of a possible self-doping effect caused by Ca deficiency, as in the case of hexaborides (*11*).

We performed the total energy calculation and found that the *P4/mbm* structure is more stable than the *I4/mcm* one, by using the full potential linear augmented plane wave method with the LDA. However, the difference is only about 8 milli-rydberg per formula unit if we use the experimentally observed lattice constants and the atomic positions in the layer. This difference is too small to definitely determine the crystal structure in the ground state. Thus, we investigated the electronic band structures for both *P4/mbm* and *I4/mcm* cases. The band structure for *P4/mbm* is semimetallic, with a small overlap (0.64 eV) between conduction and valence bands (Fig. 3). On the other hand, the *I4/mcm* structure leads to a semiconducting electronic structure with a gap of 0.43 eV. Nevertheless, as in the case of CaB_6 (*10*), the inclusion of correlation effects may bring about a semiconducting gap even in the case of the *P4/mbm* structure.

The overall features of the highest occupied molecular orbitals (HOMOs) and the lowest unoccupied molecular orbital (LUMO) do not depend on the stacking of B-C layers. Figure 4 shows the schematic view of one of the HOMOs and the LUMO for the B-C network in CaB_2C_2. The HOMO wave function consists of p_x and p_y orbitals on boron and carbon sites within a B-C layer. This accounts for the very flat valence band along the Z-Γ direction in Fig. 3. On the other hand, the LUMO wave function consists of p_z orbitals on boron and carbon sites and hybridizes well with the d_{xy} orbital on Ca sites around the Z point. Hence, the bottom of the conduction band has larger dispersion. In the case of hexaborides, the cubic symmetry gives three equivalent X points. For each X point, four borons in the same plane composing a B_6 cluster provide these orbitals. Therefore, in spite of the different compositions and crystal structures, there is a remarkable similarity between the orbitals in CaB_2C_2 and CaB_6. In both cases, the valence bands are highly anisotropic. There is another common feature in the electronic structure: The dipole transition is forbidden between the HOMO and the LUMO. This selection rule is favorable for allowing the Coulomb and exchange interactions to work, because the screening is not effective (*4*).

We emphasize that information on the wave functions in the real space is most reliable in the present band structure calculation. In contrast with the fine details in the energy band structure, which is rather sensitive to the parameters involved and to the way correlations are included, the real-space information applies to both crystal structures, *P4/mbm* and *I4/mcm*, and is insensitive to minute change of the lattice parameters. According to our calculation, the wave functions near the Fermi level of CaB_2C_2 have remarkable similarities to those in CaB_6, except for the threefold degeneracy in the latter. Therefore, peculiar

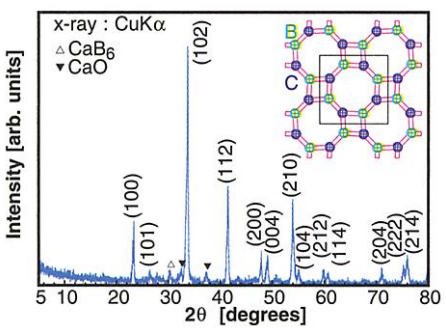

Fig. 1. Powder x-ray diffraction patterns for CaB_2C_2. The inset shows the two-dimensional B-C network in CaB_2C_2; arb., arbitrary.

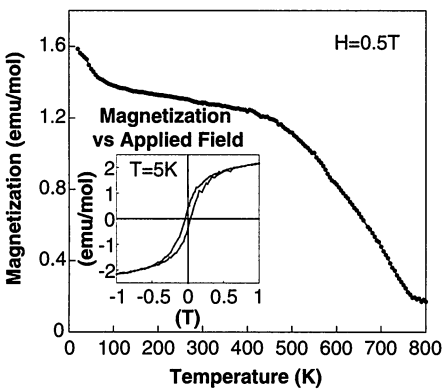

Fig. 2. Magnetization as a function of temperature in CaB_2C_2. The inset shows magnetization versus applied magnetic field.

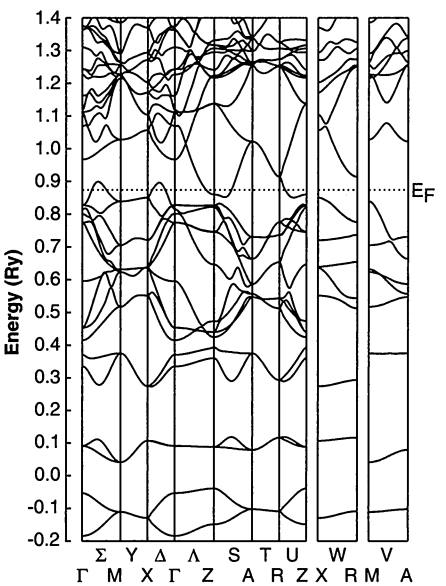

Fig. 3. Energy band structure for *P4/mbm* CaB_2C_2 along the symmetry axes. E_F denotes the Fermi level.

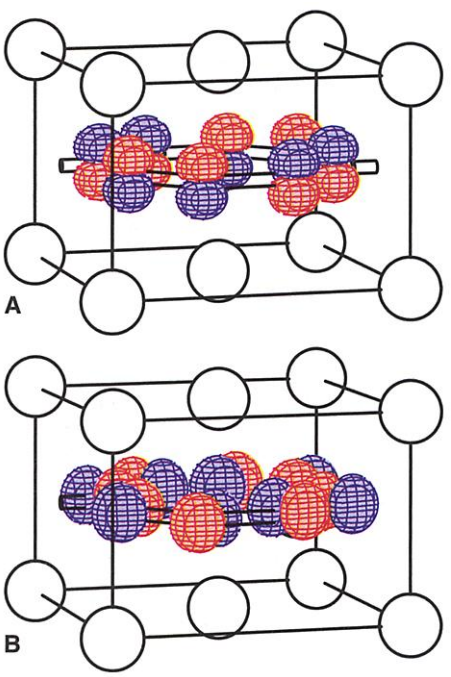

Fig. 4. Schematic view of (**A**) the LUMO and (**B**) the HOMO on the B-C network in CaB_2C_2. Red and blue indicate plus and minus in *p* wave functions, respectively, on boron and carbon sites. Large open spheres indicate Ca ions.

properties of the HOMO and the LUMO (Fig. 4) should play a crucial role in ferromagnetism in doped hexaborides and CaB_2C_2.

References and Notes

1. D. P. Young *et al.*, *Nature* **397**, 412 (1999).
2. A. Hasegawa, A. Yanase, *J. Phys. C Solid State Phys.* **12**, 5431 (1979).
3. S. Massida, A. Continenza, T. M. de Pascale, R. Monnier, *Z. Phys.* **B102**, 83 (1997).
4. M. E. Zhitomirsky, T. M. Rice, V. I. Anisimov, *Nature* **402**, 251 (1999).
5. V. Barzykin, L. P. Gor'kov, *Phys. Rev. Lett.* **84**, 1264 (2000).
6. L. Balents, C. M. Varma, *Phys. Rev. Lett.* **84**, 2207 (2000).
7. B. Albert, K. Schmitt, *Inorg. Chem.* **38**, 6159 (1999).
8. T. Onimaru, H. Onodera, K. Ohyama, H. Yamauchi, Y. Yamaguchi, *J. Phys. Soc. Jpn.* **68**, 2287 (1999).
9. J. van Duijin, K. Suzuki, J. P. Attfield, *Angew. Chem. Int. Ed.* **39**, 365 (2000).
10. H. J. Tromp *et al.*, *Phys. Rev. Lett.* **87**, 16401 (2001).
11. P. Vonlanthen *et al.*, *Phys. Rev. B* **62**, 10076 (2000).

12. Partially supported by a Grant-in-Aid for Science Research from the Ministry of Education, Culture, Sports, Science and Technology, Japan, and by a grant from the CREST.

10 April 2001; accepted 4 July 2001

Runaway Growth of Planetary Embryos Facilitated by Massive Bodies in a Protoplanetary Disk

Stephen J. Kortenkamp,[1,2]* George W. Wetherill,[2] Satoshi Inaba[2]

About 30% of detected extrasolar planets exist in multiple-star systems. The standard model of planet formation cannot easily accommodate such systems and has difficulty explaining the odd orbital characteristics of most extrasolar giant planets. We demonstrate that the formation of terrestrial-size planets may be insulated from these problems, enabling much of the framework of the standard model to be salvaged for use in complex systems. A type of runaway growth is identified that allows planetary embryos to form by a combination of nebular gas drag and perturbations from massive companions—be they giant planets, brown dwarfs, or other stars.

The standard model of planet formation (*1–3*) begins with a protoplanetary disk of gas and dust orbiting a central protostar. Growth of terrestrial planets in such a disk is usually described in three stages: (i) accretion of dust particles into 10^{12} to 10^{18} g (kilometer-size) planetesimals in $\sim 10^4$ years (*4*); (ii) gravitational accumulation of planetesimals through a process known as "runaway growth" (*5*), which produces 10^{26} to 10^{27} g (Mercury- to Mars-size) planetary embryos in $\sim 10^5$ years (*6*); and (iii) giant impacts between embryos, resulting in full-size 10^{27} to 10^{28} g terrestrial planets in $\sim 10^8$ years (*7*). Farther out in the disk, the density of solids is enhanced with condensed ices and the embryos may be capable of reaching about 10 Earth masses ($M_\oplus$) in $\sim 10^6$ years. Upon reaching this mass, the bodies may begin accumulating $\sim 10^2$ $M_\oplus$ of disk gas to form giant planets like Jupiter and Saturn in $\sim 10^7$ years (*8*). This is the "core-accretion" mechanism of giant planet formation, referring to the growth of a solid core followed by accretion of gas.

The standard model was developed to help explain how planets could have formed around our isolated Sun. However, binary stars are the most common outcome of the star formation process, and evidence exists for protoplanetary disks in young multiple-star systems (*9*). The end-state of planet formation in such systems has also been observed. Nearly 30% of the detected extrasolar planets exist in multiple-star systems (see Table 1).

The odd orbital characteristics of extrasolar giant planets are forcing considerable modifications to the standard model of planet formation. One suggestion is that giant planets like Jupiter may not form by core accretion but through a mechanism referred to as "disk instability" (*10*). Disk instability is a process involving gravitational collapse of Jupiter-mass clumps of gas and dust in a protoplanetary disk. Once an instability develops in the disk, formation of gravitationally bound giant gaseous protoplanets can occur on a time scale on the order of 100 years (*10*). This suggests that giant planets could have formed well before the runaway phase of growth of terrestrial planet embryos. The early evolution of planetesimals would then be dominated not by their own rather feeble mutual perturbations, but by much stronger perturbations from the massive planets.

As planetesimals orbit the central star, they are subject to gas drag from the protoplanetary disk. The gas in the disk is partially supported by its own pressure and orbits the star slightly slower than the Keplerian velocity. Planetesimals orbit with Keplerian velocity and, therefore, experience a head-wind drag force, the magnitude of which is inversely related to the radius of the planetesimal (*11*). As the system evolves, secular perturbations from the massive companions act to increase planetesimal eccentricities (e) and inclinations (I) while the gas drag force dissipates orbital energy, damping e and I in a way that depends on planetesimal size (*12*, *13*). Gas drag also removes angular momentum, causing planetesimal orbits to slowly decay toward the star. This size-dependent orbital decay slowly changes the relative orientation of planetesimal orbits as smaller bodies decay faster and overtake larger ones (*12*). A combination of secular perturbations and gas drag leads to a size-dependence in e and I (*12*, *13*) as well as in the phasing of the orbital orientation angles [(*12*); see also fig. 9 in (*6*)]. The size-dependent phasing of orbital elements leads to low encounter velocities between similarly sized bodies and high encounter velocities between bodies of different size.

Full-scale simulations of planetesimal growth that include mutual perturbations, secular perturbations, and gas drag are beyond the reach of current techniques. Theoretically, one would need to include $\sim 10^{12}$ small ($\sim 10^{14}$ g) planetesimals to form a single 10^{26} g embryo. Direct N-body integrations of mutually perturbing planetesimals cannot even remotely approach this figure, treating only $\sim 10^4$ bodies over the time scale required. However, existing statistical simulations of planetary growth are not limited by the number of bodies. But these simulations assume that the orbits are completely randomized, so they cannot include the size-dependent orbital phasing. We have developed a hybrid approach that capitalizes on the strengths of each technique. We use N-body integration of nonperturbing planetesimals to map the size-dependent velocity distribution and statistical simulation to follow planetesimal growth. Mutual perturbations between planetesimals are not included.

For the N-body portion we used the Wisdom-Holman (*14*) symplectic integration technique as implemented by Levison and Duncan (*15*) and modified to include gas drag (*12*, *16*). For the massive companions, we used Jupiter and Saturn with their present masses placed on orbits one astronomical unit (AU), the mean Earth-Sun distance, farther from the Sun than their current positions (i.e., Jupiter at 6.2 AU and Saturn at 10.5 AU). This was done to allow for later orbital mi-

[1]Department of Astronomy, University of Maryland, 1204 CSS Building, Stadium Drive, College Park, MD 20742–2421, USA. [2]Department of Terrestrial Magnetism, Carnegie Institution of Washington, 5241 Broad Branch Road, NW, Washington, DC 20015–1305, USA.

*To whom correspondence should be addressed. E-mail: kortenka@astro.umd.edu